PAPER

Check for updates

Carbon within carbon: growth of excitation-independent CDs within functional mesoporous carbon towards detection and adsorption of a specific nitrofuran class of antibiotics†

Sanjay Yadav,*[ab] Nishu Choudhary[ab] and Alok Ranjan Paital [ID] *[ab]

The rampant use of antibiotics has led to significant environmental pollution and the emergence of antibiotic resistance, necessitating effective detection and remediation methods. To address these pressing concerns, an innovative functional material has been developed, comprising a mesoporous matrix and a luminescent tag, both composed of carbon for the detection and removal of specific antibiotics from aqueous solutions. Initially, a high surface area bearing mesoporous carbon material with regular spherical geometry and ordered pores (5.4 nm) was synthesized and amine-functionalized with (3-aminopropyl)triethoxysilane to form OMC@NH$_2$. Subsequently, a hydrothermal process was employed to load carbon dots (CDs) *in situ* within the amine-functionalized mesoporous carbon material (CD@OMC@NH$_2$) using carbon dot precursors. The resulting blue-green luminescent material exhibited excitation-independent luminescence and demonstrated the ability to selectively detect the antibiotics nitrofurantoin (NFT) and furazolidone (FZD) through a combined effect of the IFE (inner filter effect) and FRET-based quenching mechanism. The material's detection performance was assessed by calculating the LOD (Limit of Detection), LOQ (Limit of Quantification), and L-R (Linear Range) values, which indicated its superior and sensitive detection capabilities. Moreover, the material exhibited exceptional detection parameters, a high adsorption capacity, and easy recyclability for specific antibiotics, making it a sustainable option for environmental sample monitoring.

1 Introduction

Water pollution resulting from the excessive use of antibiotics has become a serious concern, impacting water quality, public health management, and environmental monitoring systems.[1,2] Antibiotics, which are commonly used to treat diseases in humans and animals, and extensively in aquaculture, agriculture, and livestock farming, have led to their widespread presence in soil, sediments, and aquatic systems, including tap water.[3,4] This presence has adverse effects on human and animal health.[5] As a result, there is a growing focus on developing sustainable methods for monitoring and removing antibiotics from aqueous systems.[6–9] Traditional methods of detecting antibiotics include microbial inhibition, chromatography/mass spectrometry, and immunoassay techniques.[10–12] However, these methods suffer from drawbacks such as inaccuracy, time consumption, and high costs. Modern techniques like electrochemical sensing, Raman spectroscopy, and optical spectroscopy have been explored as alternatives.[6,13,14] Among them, optical methods, especially fluorescence detection of antibiotics, have garnered attention due to their high sensitivity, user-friendliness, low operational cost, and fast response.[15–19] Similarly, various remediation methods, including chemical degradation, catalytic oxidation, coagulation, membrane filtration, and adsorption, have been studied.[20–24] Among them, adsorption is considered a less expensive and effective method for the remediation process.[25,26] To achieve synergistic applications of environmental monitoring and remediation, the materials used should possess dual functions of detection and removal, along with recyclability for sustainability.[27–33] Functional mesoporous materials have been widely utilized for this purpose, as they can be loaded with fluorescence tags for detection while adsorbing the analytes. These materials offer advantages over those used for only detection or removal, as they can serve both functions in heterogeneous systems. Recently, mesoporous carbon materials have gained significant attention for various applications due to their high surface area, mesoporosity, thermal stability, and ease of functionalization.[34–37] They have been explored in sensing and adsorption studies as well.[38–41] Quantum dot-based

[a]Salt and Marine Chemicals Division, CSIR-Central Salt & Marine Chemicals Research Institute, G. B. Marg, Bhavnagar-364002, Gujarat, India. E-mail: arpaital@csmcri.res. in; sychem00700@gmail.com

[b]Academy of Scientific and Innovative Research (AcSIR), Ghaziabad-201002, India

fluorescence tags have also emerged as advantageous over organic fluorophores due to their ease of surface immobilization, cost-effectiveness, and shorter chemical processing time. Carbon dots (CDs) among quantum dots have been extensively used for different applications, including metal ion detection, photocatalysis, *in vivo* biological applications, and antibiotic detection.[42–46] However, CDs often face challenges like agglomeration, aggregation-caused quenching (ACQ) effects, and excitation dependency in aqueous media, which limit their sensing and adsorption applications. Researchers have adopted various methods like coating, doping, and *in situ* growth in the matrix to overcome these issues and protect CDs from aggregation and excitation-dependent luminescence.[31,47–49] The growth of CDs in the matrix is particularly advantageous as it eliminates the need for prior purification of CDs to achieve excitation independence. While this strategy is known for CDs in silica matrices for various applications, it has not been reported in the literature for CDs as fluorescence tags encapsulated within mesoporous carbon.

Hence, our main goal was to develop and produce a composite material consisting of carbon dots (CDs) encapsulated within an ordered mesoporous carbon (OMC) for both detection and adsorption studies. To achieve this, we started by synthesizing a high surface area mesoporous carbon using an ionic liquid-based surfactant assembly approach.[50] This synthesis method resulted in the formation of well-ordered spherical carbon spheres with a regular geometry, possessing a significant surface area of approximately 1480 $cm^3 g^{-1}$ within the mesoporous range (5.4 nm), along with a high pore volume of 1.89 $cm^3 g^{-1}$. Following the successful synthesis of the carbon nanomaterial, we chemically anchored 3-APTES ((3-aminopropyl)triethoxysilane) to the OMC, resulting in the formation of an OMC@NH$_2$ material for specific interactions at amine sites. Next, we loaded carbon dot precursors (iminodiacetic acid (IDA) and *ortho*-phenylene diamine (*o*-PD)) into the OMC@NH$_2$ material and subjected it to hydrothermal heating,

leading to the formation of a luminescent composite material known as CD@OMC@NH$_2$. This composite material exhibited unique luminescence properties. Based on the luminescence characteristics of CD@OMC@NH$_2$, we utilized it to perform two important functions: the detection and removal of specific antibiotics belonging to the nitrofuran class, such as nitrofurantoin (NFT) and furazolidone (FZD). They are 5-nitrofuran ring containing broad-spectrum antibiotics commonly used for preventing infections and as growth promoters in livestock, bee culture, and aquaculture.[51] Due to their widespread use and high elimination rate from animals, these antibiotics have become a significant source of water contamination. Although some studies have reported methods for detecting these antibiotics,[52,53] finding materials that can perform both detection and remediation functions is rare.[54] Therefore, this work encompassing a novel material for dual functions of detection and remediation of specific antibiotics with various advantages distinguishes it from existing literature.

2 Results and discussion

2.1 Structural and surface analysis

The synthetic procedure (Scheme 1) involves the synthesis of ordered mesoporous carbon spheres using Pluronic F127 surfactant as a template, an ionic liquid as a co-template, and a resol precursor (phenol + formaldehyde) as the high-density carbon source, which then gets polymerized and carbonized to give regular spherical carbon spheres. The ionic liquid principally acts as an N-dopant and nanomaterial stabilizer due to its high solubility in water and ethanol, and therefore, can direct the formation of mesostructures by interacting with the resol phase or micellar phase of F127.[50] The ratio of surfactant to ionic liquid was kept on the higher side to afford the pore in the wide mesoporous range which then can appropriately be functionalized with the entities of interest. The process yielded high surface area carbon spheres with high pore volume in the
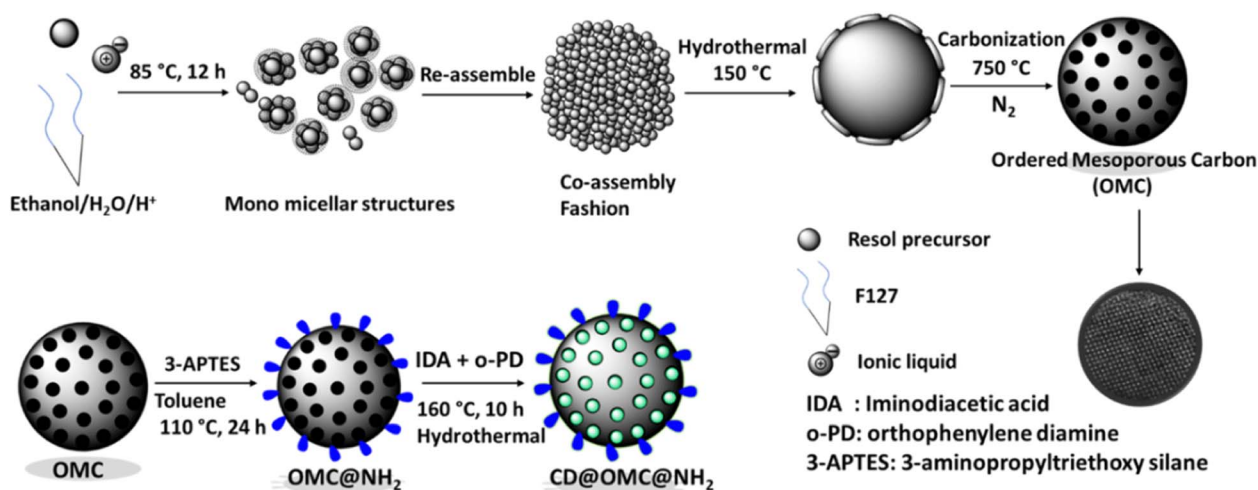
Scheme 1 The schematic representation of the synthesis of the ordered mesoporous carbon spheres (OMC), OMC@NH$_2$ and the final material CD@OMC@NH$_2$.

This journal is © The Royal Society of Chemistry 2024

J. Mater. Chem. A, 2024, **12**, 202–213 | **203**

mesoporous range, which then functionalized with 3-APTES to form the amine functionalized OMC@NH$_2$ material. The OMC@NH$_2$ material was loaded with iminodiacetic acid (IDA) and o-PD ($ortho$-phenylene diamine) and hydrothermally heated to afford the carbon dot doped final material named CD@OMC@NH$_2$ (Fig. S1†), which was then utilized for simultaneous optical detection and adsorption of specific antibiotics. A similar approach has also been reported to generate CDs in a silica matrix using SBA-NH$_2$ and carbon dot precursors (citric acid and ethylenediamine).[55]

The FeSEM images displayed regular, highly ordered, carbon spheres with a particle size of 340–490 nm with a smooth surface and good dispersion properties having a carbonaceous nature with oxygen and nitrogen contents (Fig. 1, S2 and S3†). The particle size and spherical geometry remained unaltered upon functionalization with the APTES group and also during *in situ* generation of the carbon dots; however, in the final material CD@OMC@NH$_2$ carbon spheres exhibit a rough surface probably due to the presence of the carbon dots evidenced by high magnification SEM images (Fig. 1F). The TEM and HR-TEM
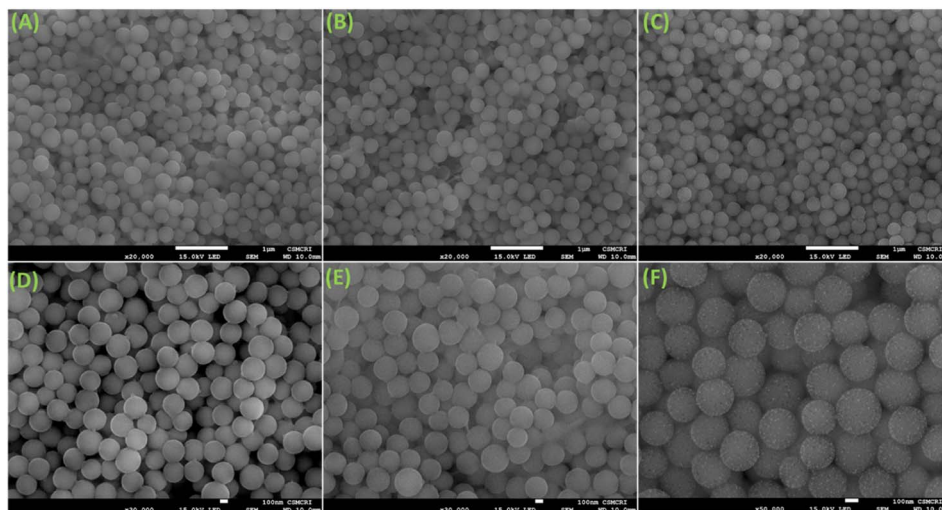

Fig. 1   (A and D) The FeSEM images of the synthesized ordered mesoporous carbon spheres (OMC); (B and E) the FeSEM images of the aminated ordered mesoporous carbon spheres (OMC@NH$_2$); (C and F) the FeSEM images of the carbon dot embedded aminated ordered mesoporous carbon spheres (CD@OMC@NH$_2$).
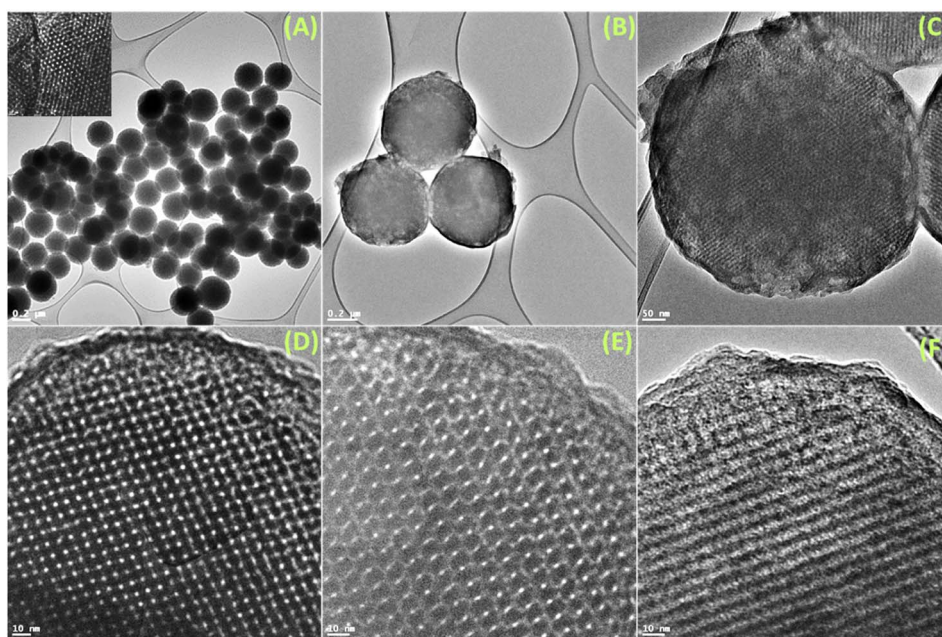

Fig. 2   (A and D) The TEM and HR-TEM images of the synthesized ordered mesoporous carbon spheres (OMC) (inset: picture showing porous nature); (B and E) the TEM and HR-TEM images of the aminated ordered mesoporous carbon spheres (OMC@NH$_2$); (C and F) the TEM and HR-TEM images of the carbon dot embedded aminated ordered mesoporous carbon spheres (CD@OMC@NH$_2$).

204 | *J. Mater. Chem. A*, 2024, **12**, 202–213

This journal is © The Royal Society of Chemistry 2024

images showed the porous nature of the carbon spheres in the mesoporous range with a regular square arrangement of the pores (Fig. 2). The pore size was significantly reduced during the covalent attachment with the APTES and completely blocked in the final material CD@OMC@NH$_2$. This is probably due to the successful functionalization process and effective encapsulation of carbon dots (Fig. 2D–F and S4†). The physiochemical parameters obtained from the N$_2$ sorption analysis (Fig. 3A) are tabulated in Table 1. The materials OMC and OMC@NH$_2$ exhibit typical type IV isotherms and type II in the final material with the highest capillary condensation in the OMC and least in the final material supporting the functionalization process (Fig. 3A). The OMC shows an extremely high surface area of 1480 cm^3 g^{-1}, pore size in the mesoporous range of order 5.43 nm, and a high pore volume of 1.89 cm^3 g^{-1}, which subsequently reduced with functionalization, supported by HR-TEM images (Fig. 2D and E). The low-angle and high-angle PXRD also gave significant information regarding the nature and pore arrangement of the carbon spheres. The high angle PXRD of the materials OMC, OMC@NH$_2$ and CD@OMC@NH$_2$ showed an amorphous nature with broad bands at 22.2, 22.8 and 22.4°, which remains nearly constant throughout the chemical processing corresponding to the (002) crystal plane (Fig. 3B, inset). The low angle PXRD of the materials showed an intense peak around 1° resembling the (100) crystal plane supporting the ordered mesoporous arrangements (Fig. 3B). Furthermore, the degree of graphitization was elucidated using the Raman profiles of the OMC material showing peaks at 1345 and 1558 cm^{-1} resembling the D band and G band arising from the graphitic carbon framework (Fig. S5†). The I_D/I_G ratio serves as a quantitative measure of disorder or imperfections in carbon-based materials, with the D-band representing disordered carbon (sp^3) and the G-band representing ordered, graphitic carbon (sp^2). For OMC, OMC@NH$_2$, and CD@OMC@NH$_2$ carbon materials, I_D/I_G ratios were determined to be 1.09, 1.13, and 0.91 respectively. The higher I_D/I_G value observed for OMC@NH$_2$, compared to bare OMC, likely stems from amination functionalization, which introduces additional structural defects (sp^3 domains) and signifies an increased level

Table 1 The physiochemical parameters of the materials from N$_2$ sorption analysis (BET)

Sample	Surface area	Pore size	Pore volume
OMC	1480.43	5.43	1.8921
OMC@NH$_2$	420.21	3.32	0.7813
CD@OMC@NH$_2$	55.31	0.23	0.0432

of disorder in OMC@NH$_2$. Conversely, the final material, CD@OMC@NH$_2$, displayed a reduced I_D/I_G ratio and an intensified I_G band intensity upon the incorporation of carbon dots (CDs). This phenomenon can be attributed to the introduction of more graphitized sp^2 domains (CDs), enhancing the degree of graphitization (crystallinity) and ultimately resulting in a lower I_D/I_G ratio due to CD doping.

The chemical analysis and surface states of the materials were investigated using various analytical techniques (Fig. 4). The FT-IR spectra of the OMC exhibited resolved peaks at 3420, 3325 2950, 1619, 1628, and 1405 cm^{-1} corresponding to –OH, –NH –CH, C=C, and C–N stretching and bending vibrations (Fig. 4A).[50] On comparing the FT-IR spectra of OMC and OMC@NH$_2$, the extra peaks at 2885, 1630, 1561, 1370, 1079 and 690 cm^{-1} correspond to the –CH$_2$ alkyl stretching of the APTES group, –NH stretching and bending vibrations and –CN linkages, whereas the peak at 1079 cm^{-1} corresponds to the Si–O–Si linkage arising from the linkage of the (3-aminopropyl)triethoxysilane group through a condensation reaction. The presence of carbon dots in the final material CD@OMC@NH$_2$ can be confirmed by the presence of peaks at 3320, 2940, 1705, 1625, 1640, 1378 and 1210 cm^{-1}, which can be assigned to –NH, –CH, C=O, C=C, C–N and C–O functionalities arising from the core and surface states of the carbon dots.

X-ray photoelectron spectroscopy (XPS) of the materials also supported the above chemical analysis. The full scan XPS spectra of the synthesized OMC showed signals of carbon (C), oxygen (O) and nitrogen (N) evidencing the carbonaceous nature of the material with the oxygen and nitrogen contents supported by EDX analysis (Fig. S6 and S3†). The chemical
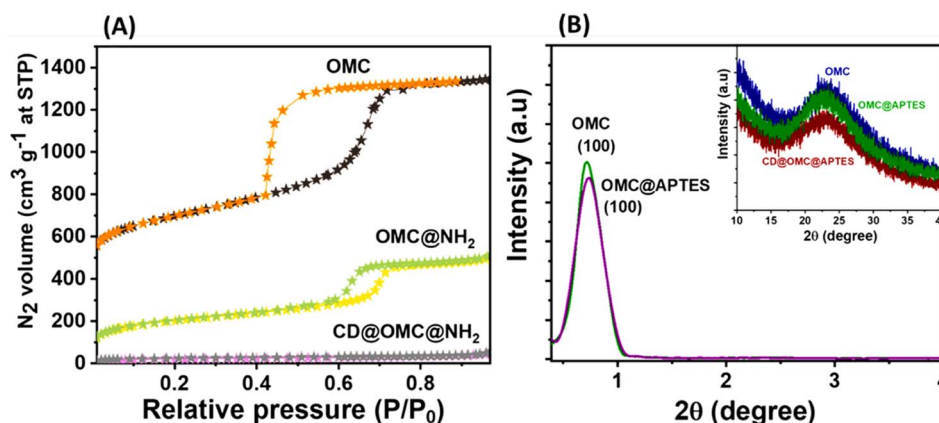
Fig. 3 (A) The S_{BET} N$_2$ sorption studies of the synthesized ordered mesoporous carbon spheres OMC, OMC@NH$_2$ and CD@OMC@NH$_2$; (B) the low-angle PXRD profiles of the ordered mesoporous carbon (OMC) and the aminated carbon spheres (OMC@NH$_2$) (inset: high angle PXRD measurements of the OMC, OMC@NH$_2$ and the final material CD@OMC@NH$_2$).
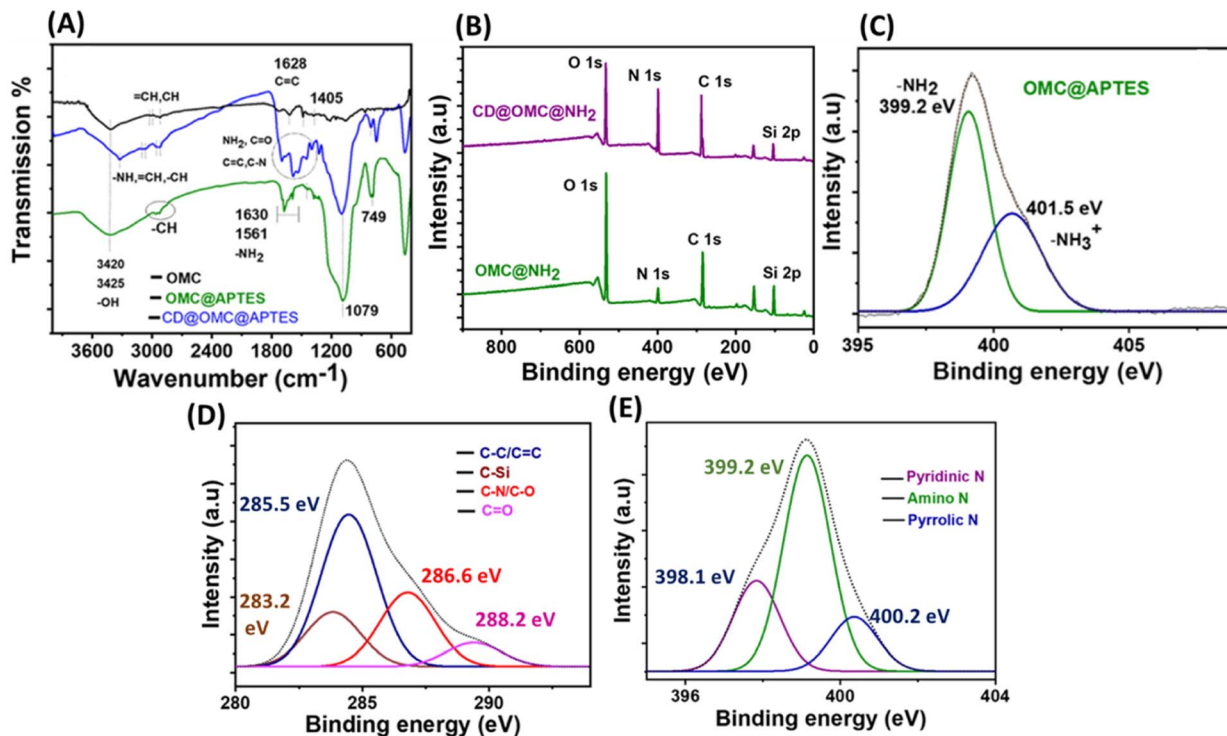
This journal is © The Royal Society of Chemistry 2024

J. Mater. Chem. A, 2024, **12**, 202–213 | **205**

Fig. 4 (A) The FTIR spectrum of the synthesized carbon materials OMC, OMC@NH$_2$ and CD@OMC@NH$_2$; (B) the comparison of the XPS full scan spectrum of the OMC@NH$_2$ and CD@OMC@NH$_2$ material: (C) the XPS N 1s core level spectrum of the aminated carbon material (OMC@NH$_2$); (D and E) the XPS C 1s and N 1s core level spectrum of the final material CD@OMC@NH$_2$.

attachment of the APTES group can be confirmed from the full scan spectrum of the material OMC@NH$_2$ showing signals of O 1s, N 1s, C 1s, and Si 2p elements. Also, the N 1s spectra can be deconvoluted into two peaks at 399.2 and 401.5 eV resembling amine functionality evidencing a successful grafting process (Fig. 4B and C). The Si–O–Si array network and intactness of Si post-APTES functionalization can be confirmed by the O 1s and Si 2p spectra of aminated OMC (OMC@NH$_2$) with peaks at 532.6 and 103.8 eV (Fig. S7†). The full scan spectrum of the final material showed peaks of the O 1s, N 1s, C 1s and Si 2p elements with an increased intensity showing greater carbon and nitrogen contents confirming the presence of carbon dots (Fig. 4B). Furthermore, the C 1s spectra can be deconvoluted into four peaks at 285.5, 283.2, 286.6 and 288.2 eV corresponding to the C=C/C–C, C–Si, C–N/C–O and C=O functionalities of the carbon dots, and also the N 1s spectra can be deconvoluted into three peaks at 398.2, 399.12 and 400.2 eV resembling pyridinic N, amino N and pyrrolic N (Fig. 4D and E), and also the Si linkage remains constant throughout the chemical processing confirmed by the full scan and core level Si 2p XPS spectra of the final material (Fig. 4B and S8†). It is observed from the above chemical analysis that the surface states of the carbon dot surface are rich in amino and ketonic groups.

2.2 Sensing and selectivity studies

To scrutinize the optical parameters and response of the material towards the analytes, selectivity experiments were performed in an aqueous buffer medium at neutral pH ∼7.4 by using UV-Vis and fluorescence spectroscopy in the dispersion state (10 mg/50 ml). From the UV-Vis spectra, it is evident that the material exhibited two characteristic bands at 288 and 350 nm possibly due to π to π* and n to π* transitions arising from the encapsulation of the carbon dot embedded in the solid matrix since the bare OMC@NH$_2$ is UV inactive (Fig. S9†). Similarly, the fluorescence studies of the material in an aqueous buffer medium show an emission band at 465 nm upon excitation at 350 nm. The material's fluorescence excitation independency was confirmed by exciting at various excitation wavelengths (345–370 nm), which showed a fixed emission band centered at 465 nm (Fig. S10†). Several antibiotics (nitrofurantoin, furazolidone, dimetridazole, theophylline, thiamphenicol, sulfamethazine, triclosan, ornidazole, and metronidazole) were screened for selective fluorescence response with the material (Fig. 5). Interestingly to our observation, the material showed selective fluorescence quenching response towards the nitrofurantoin (NFT) and furazolidone (FZD) antibiotics among other antibiotics, and no such significant fluorescence changes were observed with other antibiotics, confirming the selective nature of the material towards the sensing of NFT and FZD (Fig. 5A). However other antibiotics such as metronidazole (MDZ), dimetridazole (DTZ) and ornidazole (ODZ) showed minor fluorescence quenching following the order NFT > FZD > DTZ/MDZ > ODZ. The selective response was offered with high fluorescence quenching ∼85 and 99% with regard to FDZ and NFT validating the selective and
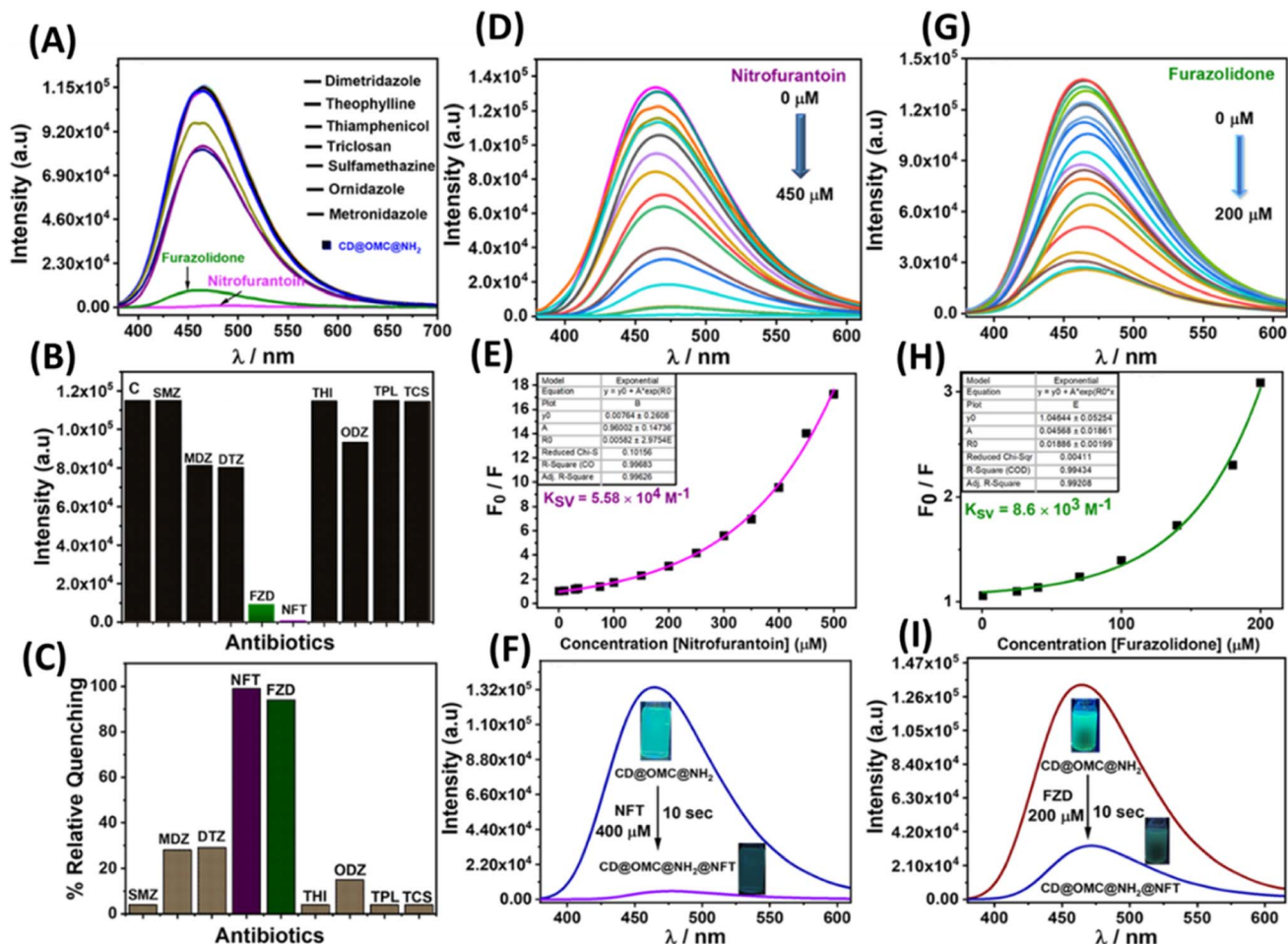
206 | *J. Mater. Chem. A*, 2024, **12**, 202–213

This journal is © The Royal Society of Chemistry 2024

Fig. 5 (A) Fluorescence selectivity studies of the material CD@OMC@NH$_2$ towards various antibiotics; (B and C) relative fluorescence emission intensity and quenching of the material with the antibiotics; (D, E, G and H) fluorescence titration profile and Stern–Volmer plot (K_{sv}) of the material with the specific antibiotics (NFT and FZD); (F and I) fluorescence response of the material with the specific antibiotics (NFT and FZD) and inset: fluorescence quenching pictures (under UV) of the final material before and after the addition of the NFT and FZD antibiotic.

sensitive response behaviour towards the specific antibiotics (Fig. 5B, C, F and I). Interference studies were also performed with an excess of other analytes except for the interfering antibiotics, where similar control results were obtained in the presence of other analytes (Fig. S11†). Furthermore, lifetime fluorescence measurements were also performed with the respective antibiotics, and time correlated single photon counting (TCSPC) spectra were obtained for the material and with the antibiotics. The fluorescence lifetime of the probe material was found to be 2.64 ns, which was significantly reduced by the addition of nitrofurantoin and furazolidone antibiotics to 1.23 and 1.63 ns respectively confirming the quenching behavior.

To determine more information regarding the sensing response, fluorescence titrations were performed with the specific antibiotics (Fig. 5D and G). The material response in sensing the antibiotics was evaluated by using the Stern–Volmer plots from the titration profiles.[31] The Stern–Volmer plots gave a non-linear regression curve towards the selective antibiotics indicating that the quenching mechanism could be static, dynamic, or a combination of both (Fig. 5E and H). The non-

linear equation can be represented as ($F_0/F = A \times E^{k[m]} + B$), where F_0 and F are the initial and final fluorescence intensities of the material, [m] is the concentration of the antibiotics, and A, B, and K are constants. The Stern–Volmer quenching constant (K_{sv}) is the product of the constants A and K in the non-linear equation. The quenching constant (K_{SV}), LOD, LOQ and linear range were calculated and are tabulated below (Table 2, Fig. S12 and S13†). For the limit of detection (LOD), a small incremental addition of the specific analytes was performed during titration profile measurement and was calculated using the 3σ method, where σ = S.D./slope, S.D. = standard deviation of the blank readings of the probe material and the slope is obtained by plotting the emission intensity *vs.* concentration of the analyte added.[27]

2.3 Fluorescence sensing mechanism

The fluorescence titration behavior of the material concerning the specific antibiotics (NFT and FZD) displayed non-linear Stern–Volmer (S–V) plots that exhibited non-linear characteristics. These outcomes indicated that the mechanism responsible for fluorescence quenching could encompass dynamic, static,

Table 2 The photophysical parameters derived from the fluorescence titration experiments

Analyte	K_{sv} (quenching constant)	LOD (nM)	LOQ (nM)	Linear range (μM)	% RSD
Nitrofurantoin (NFT)	5.58×10^4 M^{-1}	3.25	10.8	0.0108–0.36	2.78
Furazolidone (FZD)	8.63×10^3 M^{-1}	28.4	94.7	0.0947–1.2	1.89

or a combination of both processes. To enhance our understanding of this sensing mechanism, we conducted fluorescence lifetime measurements using time-correlated single photon counting (TCSPC) at varying antibiotic concentrations (Table S1†). Notably, we observed a significant reduction in the fluorescence lifetime of the probe material upon introducing the specific antibiotics. This reduction provided clear evidence of dynamic fluorescence quenching in both cases (Fig. 6A and B). Additionally, we graphed the change in fluorescence lifetime against different antibiotic concentrations (NFT and FZD), resulting in a linear relationship with an intercept at unity (Fig. 6C). The slope of this linear fit furnished the dynamic

quenching constant (K_D), calculated to be 6.0×10^5 M^{-1}. The substantial K_D value in conjunction with the non-linear S–V plots strongly corroborated the dynamic nature of the fluorescence quenching process.[56] Furthermore, this dynamic quenching process may arise from either collision interactions or the resonance energy transfer (RET) mechanism. To clarify this, we examined the spectral overlaps between the excitation and emission bands of the material with the absorbance bands of the antibiotics. Initially, we scrutinized a potential FRET (Förster resonance energy transfer) mechanism. It was observed that the emission band of the material partially coincided with the absorbance band of these antibiotics (NFT and FZD)
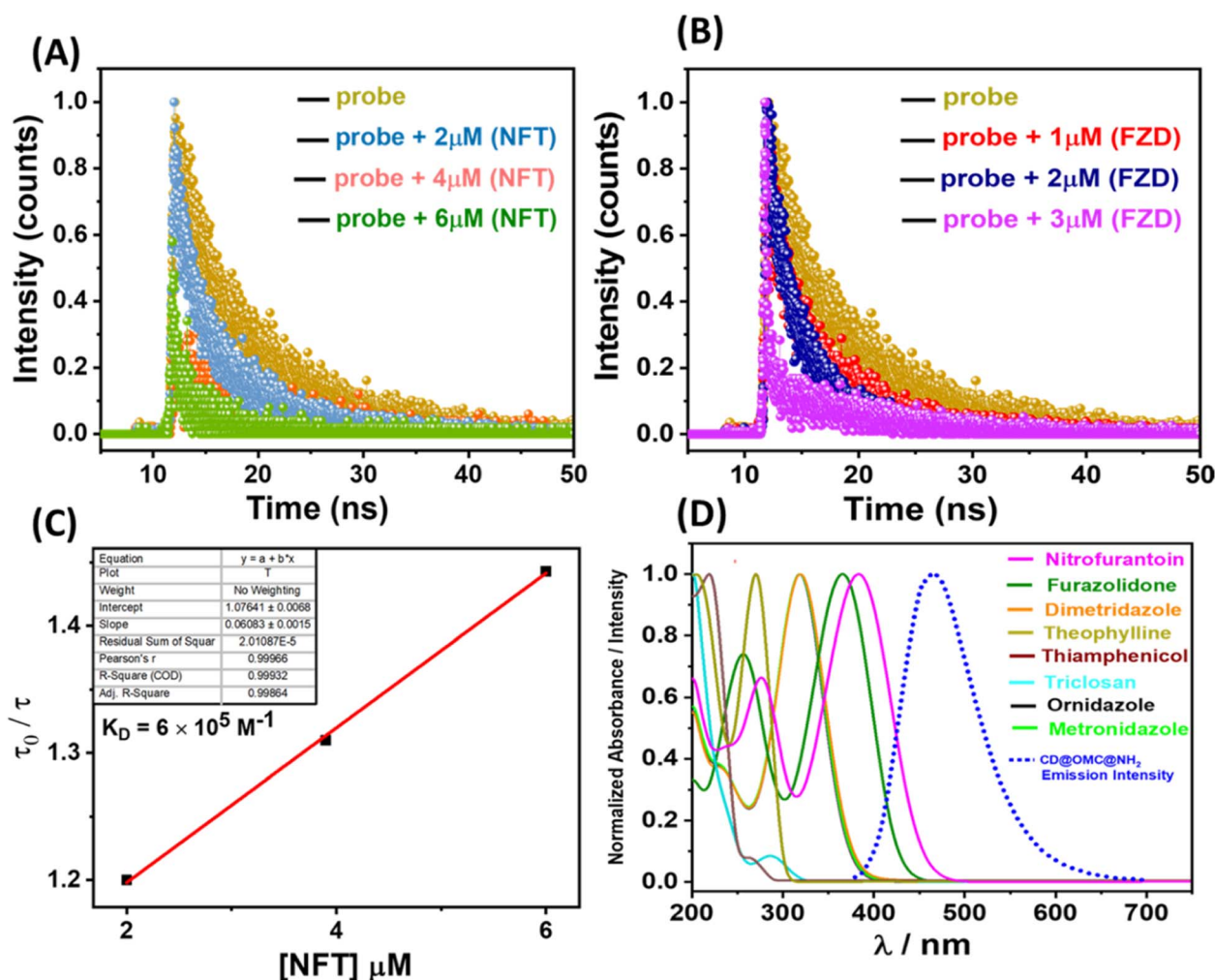
Fig. 6 (A and B) The time-correlated single photon counting (TCSPC) spectra with different concentrations of the specific antibiotic (FZD and NFT). (C) The fluorescence lifetime variation with the change in concentration of NFT; (D) the absorption and emission spectral overlap between the antibiotics and the final material exhibiting FRET.

208 | *J. Mater. Chem. A*, 2024, **12**, 202–213

This journal is © The Royal Society of Chemistry 2024

(Fig. 6D). Additionally, the presence of antibiotics had a discernible effect on the average lifetime, indicating that FRET cannot be disregarded. However, due to the comparatively less overlap between the emission band of the material and the absorbance band of these antibiotics, there might be an additional quenching effect at play. Interestingly, a significant overlap was noted between the excitation band of the material and the absorbance bands of the specific antibiotics, which facilitated the occurrence of the inner filter effect (IFE)

(Fig. S14†). This overlap signified that the energy from the excitation was absorbed by the antibiotics, resulting in the quenching of fluorescence. Thus, the IFE likely played a major role in the fluorescence quenching, and the observed emission intensity was adjusted using the equation: $F_{corr} = F_{obs} \times$ antilog $[(A_{ex} + A_{em})/2]$.[57] Here, A_{ex} and A_{em} represent the absorption at the excitation and emission wavelengths, and F_{corr} and F_{obs} denote the corrected and observed fluorescence intensities. The plot depicting the suppressed efficiencies ($E\%$) before and after
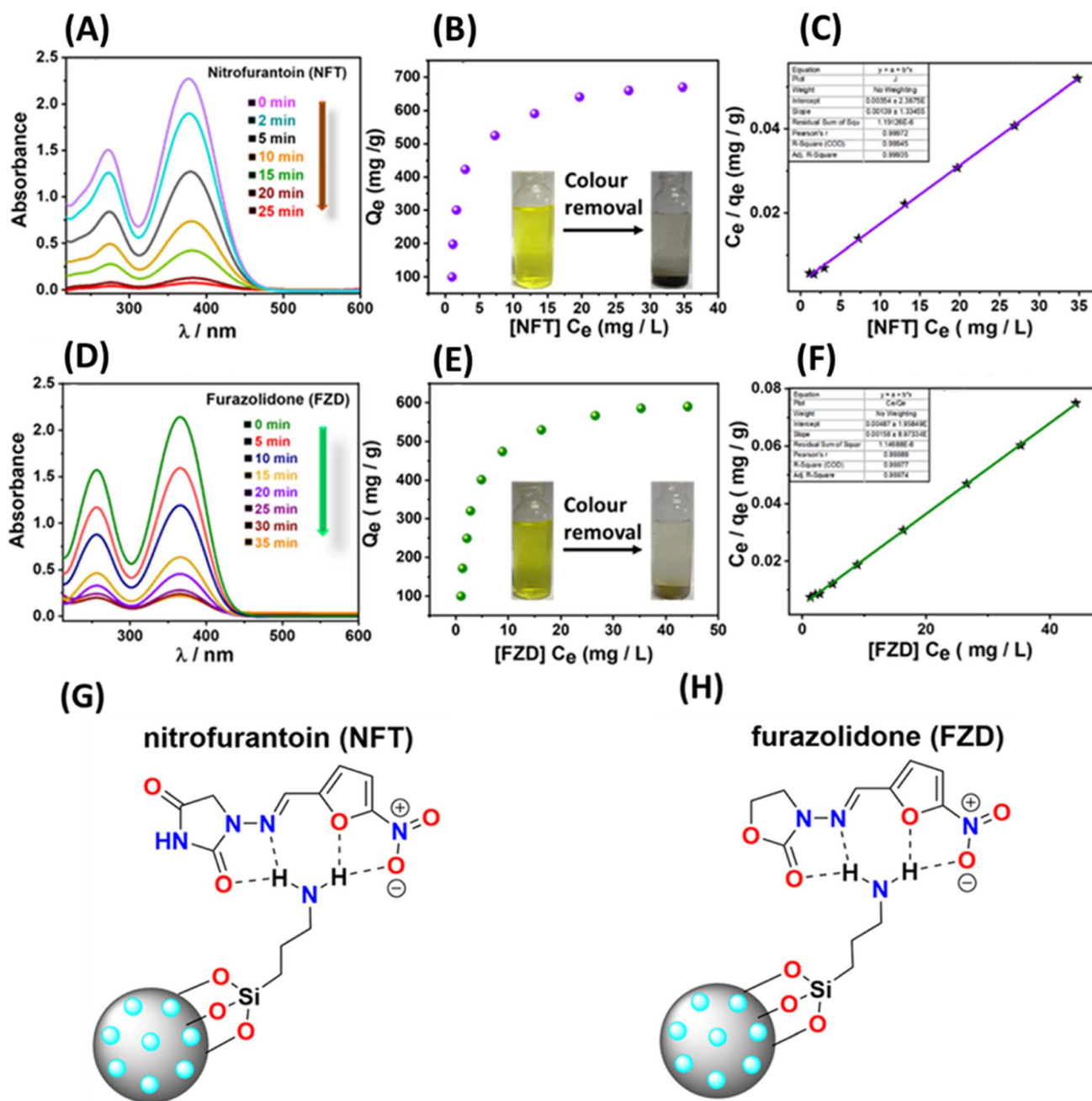
Fig. 7 (A and D) The colour removal studies of the nitrofurantoin (NFT) and furazolidone (FZD) antibiotics with the material CD@OMC@NH₂; (B and E) the equilibrium adsorption capacity (Q_e) of the material towards the specific antibiotics NFT and FZD (inset: colour removal pictures of NFT and FZD); (C and F) the Langmuir adsorption isotherm fitting of the material towards the specific antibiotics NFT and FZD. (G and H) The probable hydrogen bonding interactions of the material with the NFT and FZD antibiotic.

This journal is © The Royal Society of Chemistry 2024

J. Mater. Chem. A, 2024, **12**, 202–213 | **209**

corrections suggests that the IFE predominantly contributed to the fluorescence quenching (Fig. S15†). Hence, it is evident that both the IFE and FRET are active mechanisms for NFT and FZD, leading to a heightened level of fluorescence quenching compared to other antibiotics (MDZ, DTZ and ODZ). These latter antibiotics exhibited minor fluorescence quenching attributed solely to the IFE. Notably, the remaining antibiotics did not demonstrate any fluorescence quenching due to the absence of IFE and FRET interactions.

2.4 Adsorption studies towards the NFT and FZD antibiotics

In addition to effectively detecting antibiotics, the removal of these substances holds significant importance for environmental remediation purposes. Consequently, we conducted adsorption studies, closely monitored using UV-Vis spectroscopy. Initially, colour removal experiments were carried out by combining 5 mg of the material with 50 ml of a solution containing 30 ppm of nitrofurantoin and 50 ppm of furazolidone antibiotics. Our observations revealed that the material exhibited a rapid reduction in the antibiotic-associated colour within 25 minutes for nitrofurantoin and 35 minutes for furazolidone, respectively (Fig. 7A and D). To assess the material's adsorption capacity for these specific antibiotics, we subjected 5 mg of the material to varying concentrations of antibiotics (ranging from 5 to 50 ppm) for a duration of 4 hours, following a methodology described in our previous report.[31] Following the treatment period, the solutions were subjected to syringe filtration and subsequently analyzed using UV-Vis spectroscopy. The ultimate concentrations were ascertained utilizing calibration plots derived from UV-Vis data for the antibiotics

(Fig. S16†). The resultant adsorption isotherms were constructed and subjected to analysis to determine the equilibrium adsorption capacity (Q_e). For nitrofurantoin and furazolidone antibiotics, the equilibrium adsorption capacities (Q_e) were determined to be 685 mg g^{-1} and 590 mg g^{-1}, respectively (Fig. 7B, E and Table 3). This calculation involved the formula $Q_e = (C_i - C_e)V/W$, where Q_e represents the equilibrium adsorption capacity, C_i and C_e denote the initial and equilibrium concentrations of the specific antibiotics (in mg L^{-1}), V stands for the volume of the antibiotic solution (in liters), and W signifies the weight of the adsorbent (in grams). The notably high adsorption capacity and swift colour removal ability of these specific antibiotics are hypothesized to stem from potential hydrogen bonding interactions between the surface functional groups of the functionalized mesoporous carbon material and the electronegative atoms (O and N) present in the antibiotics (nitrofurantoin and furazolidone) (Fig. 7G and H). Similar hydrogen bonding interactions have been documented in crystal structures involving nitrofurantoin-urea dimers.[58] Moreover, the adsorption isotherms underwent analysis and were plotted, revealing a favourable fit with the Langmuir model, as indicated by a correlation factor (R^2) approaching unity (Fig. 7C and F).

2.5 Regeneration and reusability studies

Due to escalating environmental concerns, a pronounced emphasis has been placed on the recycling of materials in a manner that aligns with eco-friendly practices, thereby promoting sustainability. Preliminary efforts to eliminate these adsorbed antibiotics using solvents such as methanol and

Table 3 Adsorption parameters of the material

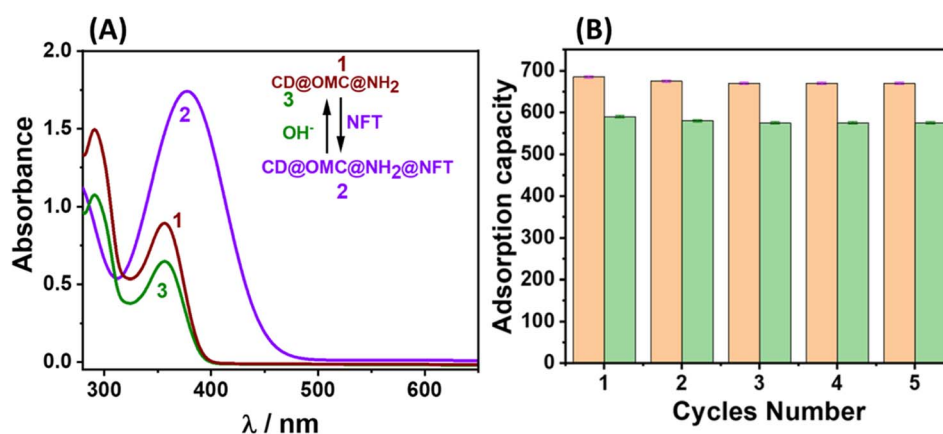| Analyte	Experimental (Q_e) (mg g^{-1})	Langmuir linear isotherm		
		Q_{max} (mg g^{-1})	K_L [L g^{-1}]	R^2
Nitrofurantoin (NFT)	685	719.42	0.392	0.99
Furazolidone (FZD)	590	632.91	0.324	0.99

Fig. 8 (A) The UV-Vis tracking of the regeneration of the final material with basic aqueous solution; (B) the adsorption capacity of the material up to 5 cycles towards the NFT and FZD antibiotics.

210 | J. Mater. Chem. A, 2024, 12, 202–213

This journal is © The Royal Society of Chemistry 2024

acetone exhibited protracted time requirements and proved inadequate in achieving complete removal, even with repeated washes. Nevertheless, by employing a basic aqueous solution (0.1 N NaOH), a notably efficient removal of these antibiotics was accomplished, an outcome that was closely tracked using UV-Vis spectroscopy (Fig. 8). This efficacy can perhaps be attributed to the hydroxyl anions disrupting the robust hydrogen bonding interactions between amines and the antibiotics, thus facilitating the expeditious removal of the adsorbed antibiotics. Subsequently, the sorption behaviour of the regenerated material towards the specific analytes was meticulously examined for 5 cycles, with the corresponding adsorption capacity meticulously quantified (Fig. 8B). Comprehensive characterization endeavors confirmed that the regenerated material displayed functional, structural, and optical properties that closely mirrored those of the original material (Fig S17†). This congruence in properties implies a straightforward and uncomplicated recovery process for the material.

3 Experimental section

3.1 Synthesis of ordered mesoporous carbon (OMC)

Initially, the resol precursor was synthesized according to a literature report.[59] After the synthesis of the resol precursor, it was transferred to ethanol, and the aqueous solution of [Bmim]Cl (0.5 g in 80 ml water) was added slowly and heated at 85 °C for 12 h followed by hydrothermally heating at 150 °C for 10 h. After the hydrothermal heating, the product was collected by centrifugation at 8000 rpm for 3 min and carbonized in an inert atmosphere at 750 °C for 24 h and named OMC.

3.2 Synthesis of OMC@NH₂

For the amination of the above synthesized OMC, typically 1 g of the OMC was refluxed with 4 ml of (3-aminopropyl)triethoxysilane (3-APTES) at 110 °C for 24 h. Afterward, the material was collected by centrifugation and washed thoroughly with toluene and chloroform 3 times and finally dried in an oven at 60 °C for 2 h obtaining 1.13 g of the product named OMC@NH₂.

3.3 Synthesis of the final material CD@OMC@NH₂

For the synthesis of the final material CD@OMC@NH₂, the carbon dot precursors (iminodiacetic acid (IDA), 0.5 g and o-phenylenediamine (o-PD), 0.5 g) were hydrothermally heated with 1 g of the above-aminated material for 10 h at 160 °C in 40 ml water. The product was collected by centrifugation and washed thoroughly with water and methanol and dried in an oven at 60 °C for 2 h obtaining 1.24 g of the final product named CD@OMC@NH₂.

3.4 Sensing studies

Photophysical investigations were conducted by preparing an aqueous dispersion of the material at a concentration of 10 mg per 50 ml. The suspension was vigorously mixed before each spectral measurement. Antibiotics screened for selectivity studies are nitrofurantoin, furazolidone, dimetridazole, theophylline, thiamphenicol, sulfamethazine, triclosan, ornidazole and metronidazole. The UV-Vis spectra were recorded in the range of 200 to 800 nm, while fluorescence analyses were carried out between 300 and 700 nm, with an excitation wavelength of 350 nm. For determining the limit of detection (LOD) and limit of quantification (LOQ), the 3σ and 10σ methods were utilized. This involved progressively adding small quantities of different specific antibiotics (NFT and FZD) in titration experiments.

3.5 Adsorption studies

To explore the adsorption capabilities of the material towards the specific antibiotics, a series of batch adsorption experiments were conducted. Initially, varying concentrations (5–50 ppm) of specific antibiotic solutions were prepared and their UV-Vis spectra were recorded to plot the calibration plots. Then 5 mg of materials were added separately to the above antibiotic solutions and the sample tubes were agitated for a duration of 3 to 4 hours. Once the treatment phase was complete, the tubes were subjected to centrifugation, and again UV-Vis spectra of the solutions were recorded. The final concentrations were determined from the calibration curves of absorbance vs. concentrations of the specific antibiotics. The equilibrium adsorption capacity (Q_e) was ascertained from the adsorption isotherm, employing the formula $Q_e = (C_i - C_e)V/W$, where C_i represents the initial concentration, C_e is the final concentration, V signifies the volume, and W stands for the weight of the material. The acquired experimental data were subjected to analysis using the Langmuir and Freundlich adsorption isotherms.

4 Conclusions

In essence, this study is dedicated to developing an innovative functional material that serves a dual role: detecting and adsorbing particular antibiotics. This material comprises two carbon-based constituents: mesoporous carbon as the substrate and carbon dots functioning as fluorescent markers. Notably, this combination has not been explored before for detection investigations. The initial step involved creating precisely shaped spherical mesoporous carbon structures with pores measuring around 5 nm. These structures were subsequently endowed with amine groups on their surfaces. Using a hydrothermal process, carbon dots were incorporated into the amine-functionalized mesoporous carbon matrix using carbon dot precursors. The resulting composite emitted blue-green luminescence consistently, regardless of alterations in excitation conditions, providing a distinct advantage for sensing applications. Effectively, this material identified the presence of antibiotics like nitrofurantoin (NFT) and furazolidone (FZD) by relying on a combined effect of the IFE and FRET-based quenching mechanism. Its performance was assessed by establishing the limits of detection (LOD) and quantification (LOQ), underscoring its impressive sensitivity and precise detection capability. Moreover, the material exhibited a robust adsorption process for these antibiotics and could be conveniently regenerated, representing a sustainable substitute for

This journal is © The Royal Society of Chemistry 2024

J. Mater. Chem. A, 2024, **12**, 202–213 | **211**

functional materials that employ expensive organic fluorophores for detection purposes. The added advantage of emission that remains consistent regardless of excitations (excitation-independent) distinguishes it from typical carbon dots, which often encounter issues like aggregation and excitation-dependent luminescence. Considering these myriad benefits, this material stands as an environmentally viable choice for continuous monitoring and elimination of specific antibiotics such as nitrofurans.

Author contributions

The manuscript was written through the contribution of all the authors. All the authors have approved the final versions of the manuscript.

Conflicts of interest

The authors declare no competing financial interest.

Acknowledgements

References

1 R. Gothwal and T. Shashidhar, *Clean: Soil, Air, Water*, 2015, **43**, 479–489.

2 M. Patel, R. Kumar, K. Kishor, T. Mlsna, C. U. Pittman and D. Mohan, *Chem. Rev.*, 2019, **119**, 3510–3673.

3 K. Kümmerer, *Chemosphere*, 2009, **75**, 417–434.

4 Y. Valcárcel, S. González Alonso, J. L. Rodríguez-Gil, A. Gil and M. Catalá, *Chemosphere*, 2011, **84**, 1336–1348.

5 M.-C. Danner, A. Robertson, V. Behrends and J. Reiss, *Sci. Total Environ.*, 2019, **664**, 793–804.

6 Q. Wang and W.-M. Zhao, *Sens. Actuators, B*, 2018, **269**, 238–256.

7 D. Mangla, Annu, A. Sharma and S. Ikram, *J. Hazard. Mater.*, 2022, **425**, 127946.

8 P. Darvishi, S. A. Mousavi, A. Mahmoudi and D. Nayeri, *Environ. Sci.: Water Res. Technol.*, 2023, **9**, 11–37.

9 A. S. Oberoi, Y. Jia, H. Zhang, S. K. Khanal and H. Lu, *Environ. Sci. Technol.*, 2019, **53**, 7234–7264.

10 M. G. Pikkemaat, M. L. B. A. Rapallini, T. Zuidema, J. W. A. Elferink, S. Oostra-van Dijk and W. D. M. Driessen-van Lankveld, *Food Addit. Contam.: Part A*, 2011, **28**, 26–34.

11 S. Saito-Shida, T. Hayashi, S. Nemoto and H. Akiyama, *Food Chem.*, 2018, **249**, 84–90.

12 D. Kong, Z. Xie, L. Liu, S. Song, H. Kuang and C. Xu, *Food Agric. Immunol.*, 2017, **28**, 414–426.

13 R. Nehru, C.-D. Dong and C.-W. Chen, *ACS Appl. Nano Mater.*, 2021, **4**, 6768–6777.

14 D. Yan, J. Popp, M. W. Pletz and T. Frosch, *ACS Photonics*, 2017, **4**, 138–145.

15 P. Raja Lakshmi, P. Nanjan, S. Kannan and S. Shanmugaraju, *Coord. Chem. Rev.*, 2021, **435**, 213793.

16 D. Zhao, X.-H. Liu, Y. Zhao, P. Wang, Y. Liu, M. Azam, S. I. Al-Resayes, Y. Lu and W.-Y. Sun, *J. Mater. Chem. A*, 2017, **5**, 15797–15807.

17 X. Liu, B. Liu, G. Li and Y. Liu, *J. Mater. Chem. A*, 2018, **6**, 17177–17185.

18 Y. Tang, M. Zheng, W. Xue, H. Huang and G. Zhang, *ACS Appl. Mater. Interfaces*, 2022, **14**, 37853–37864.

19 Z. Meng, F. Yang, X. Wang, W.-L. Shan, D. Liu, L. Zhang and G. Yuan, *Inorg. Chem.*, 2023, **62**, 1297–1305.

20 M. Pirsaheb, H. Hossaini and H. Janjani, *Microchem. J.*, 2020, **153**, 104430.

21 T. Saitoh, K. Shibata, K. Fujimori and Y. Ohtani, *Sep. Purif. Technol.*, 2017, **187**, 76–83.

22 E. M. Cuerda-Correa, M. F. Alexandre-Franco and C. Fernández-González, *Water*, 2019, **12**, 102.

23 J. J. S. Alonso, N. El Kori, N. Melián-Martel and B. Del Río-Gamero, *J. Environ. Manage.*, 2018, **217**, 337–345.

24 D. Nayeri, S. A. Mousavi and A. Mehrabi, *J. Appl. Res. Water Wastewater*, 2019, **6**, 67–72.

25 L. Ji, F. Liu, Z. Xu, S. Zheng and D. Zhu, *Environ. Sci. Technol.*, 2010, **44**, 3116–3122.

26 X. Zhang, J. Shen, N. Zhuo, Z. Tian, P. Xu, Z. Yang and W. Yang, *ACS Appl. Mater. Interfaces*, 2016, **8**, 24273–24280.

27 S. Chatterjee and A. R. Paital, *Adv. Funct. Mater.*, 2018, **28**, 1704726.

28 S. Yadav, N. Choudhary, M. Ranjan Dash and A. Ranjan Paital, *Chem. Eng. J.*, 2022, **450**, 138042.

29 B. Wang, X.-L. Lv, D. Feng, L.-H. Xie, J. Zhang, M. Li, Y. Xie, J.-R. Li and H.-C. Zhou, *J. Am. Chem. Soc.*, 2016, **138**, 6204–6216.

30 S. Yadav, N. Choudhary and A. R. Paital, *Carbon*, 2023, **205**, 527–539.

31 S. Yadav, N. Choudhary, V. Sonpal and A. Ranjan Paital, *Chem. Eng. J.*, 2023, **471**, 144715.

32 A. H. Malik and P. K. Iyer, *ACS Appl. Mater. Interfaces*, 2017, **9**, 4433–4439.

33 D. Dai, J. Yang, Y. Wang and Y. Yang, *Adv. Funct. Mater.*, 2021, **31**, 2006168.

34 M. R. Benzigar, S. N. Talapaneni, S. Joseph, K. Ramadass, G. Singh, J. Scaranto, U. Ravon, K. Al-Bahily and A. Vinu, *Chem. Soc. Rev.*, 2018, **47**, 2680–2721.

35 R. Chakraborty, V. K, M. Pradhan and A. K. Nayak, *J. Mater. Chem. A*, 2022, **10**, 6965–7005.

36 G. P. Mane, D. S. Dhawale, C. Anand, K. Ariga, Q. Ji, M. A. Wahab, T. Mori and A. Vinu, *J. Mater. Chem. A*, 2013, **1**, 2913.

37 Y. Liu, Z. Wang, W. Teng, H. Zhu, J. Wang, A. A. Elzatahry, D. Al-Dahyan, W. Li, Y. Deng and D. Zhao, *J. Mater. Chem. A*, 2018, **6**, 3162–3170.

38 J. Górka, R. T. Mayes, L. Baggetto, G. M. Veith and S. Dai, *J. Mater. Chem. A*, 2013, **1**, 3016.

39 D. Saha, S. Barakat, S. E. Van Bramer, K. A. Nelson, D. K. Hensley and J. Chen, *ACS Appl. Mater. Interfaces*, 2016, **8**, 34132–34142.

212 | *J. Mater. Chem. A*, 2024, **12**, 202–213

This journal is © The Royal Society of Chemistry 2024

40 Y. Shen, Z. Xin, Y. Zhu and J. Wang, *Sens. Actuators, B*, 2022, **358**, 131485.

41 C. Li, Y. Meng, S. Wang, M. Qian, J. Wang, W. Lu and R. Huang, *ACS Nano*, 2015, **9**, 12096–12103.

42 C. Long, Z. Jiang, J. Shangguan, T. Qing, P. Zhang and B. Feng, *Chem. Eng. J.*, 2021, **406**, 126848.

43 I. Kaur, V. Batra, N. Kumar Reddy Bogireddy, S. D. Torres Landa and V. Agarwal, *Food Chem.*, 2023, **406**, 135029.

44 M. Li, T. Chen, J. J. Gooding and J. Liu, *ACS Sens.*, 2019, **4**, 1732–1748.

45 L. Qiao, S. Qian, Y. Wang, S. Yan and H. Lin, *Chem. –Eur. J.*, 2018, **24**, 4703–4709.

46 R. Purbia, Y. M. Kwon, H.-D. Kim, Y. S. Lee, H. Shin and J. M. Baik, *J. Mater. Chem. A*, 2020, **8**, 11734–11742.

47 J. Chen, G. Xiao, G. Duan, Y. Wu, X. Zhao and X. Gong, *Chem. Eng. J.*, 2021, **421**, 127743.

48 Y. Luo, S. Fan, W. Yu, Z. Wu, D. A. Cullen, C. Liang, J. Shi and C. Su, *Adv. Mater.*, 2018, **30**, 1704576.

49 Y. Tian, Z. Ran and W. Yang, *RSC Adv.*, 2017, **7**, 43839–43844.

50 X. Zhao, S. Li, H. Cheng, J. Schmidt and A. Thomas, *ACS Appl. Mater. Interfaces*, 2018, **10**, 3912–3920.

51 A. Zdarta, W. Smułek, Z. Bielan, J. Zdarta, L. N. Nguyen, A. Zgoła-Grześkowiak, L. D. Nghiem, T. Jesionowski and E. Kaczorek, *Bioresour. Technol.*, 2021, **339**, 125577.

52 S. Zhou, L. Lu, D. Liu, J. Wang, H. Sakiyama, M. Muddassir, A. Nezamzadeh-Ejhieh and J. Liu, *CrystEngComm*, 2021, **23**, 8043–8052.

53 Z. Cong, Z. Song, Y. Ma, M. Zhu, Y. Zhang, S. Wu and E. Gao, *Chem. – Asian J.*, 2021, **16**, 1773–1779.

54 P. Su, A. Zhang, L. Yu, H. Ge, N. Wang, S. Huang, Y. Ai, X. Wang and S. Wang, *Sens. Actuators, B*, 2022, **350**, 130865.

55 Z. Wang, C. Xu, Y. Lu, F. Wu, G. Ye, G. Wei, T. Sun and J. Chen, *ACS Appl. Mater. Interfaces*, 2017, **9**, 7392–7398.

56 A. S. Tanwar, R. Parui, R. Garai, M. A. Chanu and P. K. Iyer, *ACS Meas. Sci. Au*, 2022, **2**, 23–30.

57 S. Chen, Y.-L. Yu and J.-H. Wang, *Anal. Chim. Acta*, 2018, **999**, 13–26.

58 D. A. Zhu, G. G. Z. Zhang, K. L. S. T. George and D. Zhou, *J. Pharm. Sci.*, 2011, **100**, 3529–3538.

59 Y. Meng, D. Gu, F. Zhang, Y. Shi, H. Yang, Z. Li, C. Yu, B. Tu and D. Zhao, *Angew. Chem., Int. Ed.*, 2005, **44**, 7053–7059.

This journal is © The Royal Society of Chemistry 2024

J. Mater. Chem. A, 2024, **12**, 202–213 | **213**